Femtogram dispersive L3-nanobeam optomechanical cavities: design and experimental comparison

Jiangjun Zheng,[1,3,*] Xiankai Sun,[2,3] Ying Li,[1] Menno Poot,[2] Ali Dadgar,[1] Norman Nan Shi,[1] Hong X. Tang,[2] and Chee Wei Wong[1,*]

[1]*Optical Nanostructures Laboratory, Columbia University, New York, New York 10027, USA*
[2]*Department of Electrical Engineering, Yale University, New Haven, Connecticut 06511, USA*
[3]*These authors contributed equally to this work*
[*]*cww2104@columbia.edu*

Abstract: We present the design and experimental comparison of femtogram L3-nanobeam photonic crystal cavities for optomechanical studies. Two symmetric nanobeams are created by placing three air slots in a silicon photonic crystal slab where three holes are removed. The nanobeams' mechanical frequencies are higher than 600 MHz with ultrasmall effective modal masses at approximately 20 femtograms. The optical quality factor (Q) is optimized up to 53,000. The optical and mechanical modes are dispersively coupled with a vacuum optomechanical coupling rate $g_0/2\pi$ exceeding 200 kHz. The anchor-loss-limited mechanical Q of the differential beam mode is evaluated to be greater than 10,000 for structures with ideally symmetric beams. The influence of variations on the air slot width and position is also investigated. The devices can be used as ultrasensitive sensors of mass, force, and displacement.

©2012 Optical Society of America

OCIS codes: (220.4880) Optomechanics; (230.5750) Resonators; (230.5298) Photonic crystals.

References and links

1. T. J. Kippenberg and K. J. Vahala, "Cavity optomechanics: back-action at the mesoscale," Science **321**(5893), 1172–1176 (2008).
2. I. Favero and K. Karrai, "Optomechanics of deformable optical devices," Nat. Photonics **3**(4), 201–205 (2009).
3. D. Van Thourhout and J. Roels, "Optomechanical device actuation through the optical gradient force," Nat. Photonics **4**(4), 211–217 (2010).
4. F. Marquardt, "Optomechanics: push towards the quantum limit," Nat. Phys. **4**(7), 513–514 (2008).
5. E. Verhagen, S. Deléglise, S. Weis, A. Schliesser, and T. J. Kippenberg, "Quantum-coherent coupling of a mechanical oscillator to an optical cavity mode," Nature **482**(7383), 63–67 (2012).
6. J. Chan, T. P. M. Alegre, A. H. Safavi-Naeini, J. T. Hill, A. Krause, S. Gröblacher, M. Aspelmeyer, and O. Painter, "Laser cooling of a nanomechanical oscillator into its quantum ground state," Nature **478**(7367), 89–92 (2011).
7. J. D. Teufel, T. Donner, D. Li, J. W. Harlow, M. S. Allman, K. Cicak, A. J. Sirois, J. D. Whittaker, K. W. Lehnert, and R. W. Simmonds, "Sideband cooling of micromechanical motion to the quantum ground state," Nature **475**(7356), 359–363 (2011).
8. J. C. Sankey, C. Yang, B. M. Zwickl, A. M. Jayich, and J. G. E. Harris, "Strong and tunable nonlinear optomechanical coupling in a low-loss system," Nat. Phys. **6**(9), 707–712 (2010).
9. A. D. O'Connell, M. Hofheinz, M. Ansmann, R. C. Bialczak, M. Lenander, E. Lucero, M. Neeley, D. Sank, H. Wang, M. Weides, J. Wenner, J. M. Martinis, and A. N. Cleland, "Quantum ground state and single-phonon control of a mechanical resonator," Nature **464**(7289), 697–703 (2010).
10. Y.-S. Park and H. Wang, "Resolved-sideband and cryogenic cooling of an optomechanical resonator," Nat. Phys. **5**(7), 489–493 (2009).
11. S. Gröblacher, J. B. Hertzberg, M. R. Vanner, G. D. Cole, S. Gigan, K. C. Schwab, and M. Aspelmeyer, "Demonstration of an ultracold micro-optomechanical oscillator in a cryogenic cavity," Nat. Phys. **5**(7), 485–488 (2009).
12. A. Schliesser, R. Rivière, G. Anetsberger, O. Arcizet, and T. J. Kippenberg, "Resolved-sideband cooling of a micromechanical oscillator," Nat. Phys. **4**(5), 415–419 (2008).
13. I. Wilson-Rae, P. Zoller, and A. Imamoğlu, "Laser cooling of a nanomechanical resonator mode to its quantum ground state," Phys. Rev. Lett. **92**(7), 075507 (2004).

14. S. Weis, R. Rivière, S. Deléglise, E. Gavartin, O. Arcizet, A. Schliesser, and T. J. Kippenberg, "Optomechanically induced transparency," Science **330**(6010), 1520–1523 (2010).
15. A. H. Safavi-Naeini, T. P. Mayer Alegre, J. Chan, M. Eichenfield, M. Winger, Q. Lin, J. T. Hill, D. E. Chang, and O. Painter, "Electromagnetically induced transparency and slow light with optomechanics," Nature **472**(7341), 69–73 (2011).
16. G. Bahl, M. Tomes, F. Marquardt, and T. Carmon, "Observation of spontaneous Brillouin cooling," Nat. Phys. **8**(3), 203–207 (2012).
17. C. A. Regal, J. D. Teufel, and K. W. Lehnert, "Measuring nanomechanical motion with a resonant microwave cavity interferometer," Nat. Phys. **4**(7), 555–560 (2008).
18. V. Fiore, Y. Yang, M. C. Kuzyk, R. Barbour, L. Tian, and H. Wang, "Storing optical information as a mechanical excitation in a silica optomechanical resonator," Phys. Rev. Lett. **107**(13), 133601 (2011).
19. G. Anetsberger, E. Gavartin, O. Arcizet, Q. P. Unterreithmeier, E. M. Weig, M. L. Gorodetsky, J. P. Kotthaus, and T. J. Kippenberg, "Measuring nanomechanical motion with an imprecision far below the standard quantum limit," Phys. Rev. A **82**, 061804(R) (2010).
20. G. Khitrova, H. M. Gibbs, M. Kira, S. W. Koch, and A. Scherer, "Vacuum Rabi splitting in semiconductors," Nat. Phys. **2**(2), 81–90 (2006).
21. I. Fushman, D. Englund, A. Faraon, N. Stoltz, P. Petroff, and J. Vuckovic, "Controlled phase shifts with a single quantum dot," Science **320**(5877), 769–772 (2008).
22. P. Colman, C. Husko, S. Combrie, I. Sagnes, C. W. Wong, and A. De Rossi, "Temporal solitons and pulse compression in photonic crystal waveguides," Nat. Photonics **4**(12), 862–868 (2010).
23. J. F. McMillan, M. Yu, D.-L. Kwong, and C. W. Wong, "Observation of four-wave mixing in slow-light silicon photonic crystal waveguides," Opt. Express **18**(15), 15484–15497 (2010).
24. J. F. McMillan, M. Yu, D.-L. Kwong, and C. W. Wong, "Observations of spontaneous Raman scattering in silicon slow-light photonic crystal waveguides," Appl. Phys. Lett. **93**(25), 251105 (2008).
25. M. Notomi, H. Taniyama, S. Mitsugi, and E. Kuramochi, "Optomechanical wavelength and energy conversion in high- Q double-layer cavities of photonic crystal slabs," Phys. Rev. Lett. **97**(2), 023903 (2006).
26. Y. Li, J. Zheng, J. Gao, J. Shu, M. S. Aras, and C. W. Wong, "Design of dispersive optomechanical coupling and cooling in ultrahigh-Q/V slot-type photonic crystal cavities," Opt. Express **18**(23), 23844–23856 (2010).
27. M. Li, W. H. P. Pernice, C. Xiong, T. Baehr-Jones, M. Hochberg, and H. X. Tang, "Harnessing optical forces in integrated photonic circuits," Nature **456**(7221), 480–484 (2008).
28. M. Bagheri, M. Poot, M. Li, W. P. H. Pernice, and H. X. Tang, "Dynamic manipulation of nanomechanical resonators in the high-amplitude regime and non-volatile mechanical memory operation," Nat. Nanotechnol. **6**(11), 726–732 (2011).
29. G. S. Wiederhecker, L. Chen, A. Gondarenko, and M. Lipson, "Controlling photonic structures using optical forces," Nature **462**(7273), 633–636 (2009).
30. M. Eichenfield, R. Camacho, J. Chan, K. J. Vahala, and O. Painter, "A picogram- and nanometre-scale photonic-crystal optomechanical cavity," Nature **459**(7246), 550–555 (2009).
31. J. Zheng, Y. Li, M. S. Aras, A. Stein, K. L. Shepard, and C. W. Wong, "Parametric optomechanical oscillations in two-dimensional slot-type high-Q photonic crystal cavities," Appl. Phys. Lett. **100**(21), 211908 (2012).
32. A. H. Safavi-Naeini, T. P. M. Alegre, M. Winger, and O. Painter, "Optomechanics in an ultrahigh-Q two-dimensional photonic crystal cavity," Appl. Phys. Lett. **97**(18), 181106 (2010).
33. E. Gavartin, R. Braive, I. Sagnes, O. Arcizet, A. Beveratos, T. J. Kippenberg, and I. Robert-Philip, "Optomechanical coupling in a two-dimensional photonic crystal defect cavity," Phys. Rev. Lett. **106**(20), 203902 (2011).
34. X. Sun, J. Zheng, M. Poot, C. W. Wong, and H. X. Tang, "Femtogram doubly clamped nanomechanical resonators embedded in a high-Q two-dimensional photonic crystal nanocavity," Nano Lett. **12**(5), 2299–2305 (2012), doi:10.1021/nl300142t
35. D. Bindel and S. Govindjee, "Elastic PMLs for resonator anchor loss simulation," Tech report UCB / SEMM-2005/01.
36. U. Basu and A. K. Chopra, "Perfectly matched layers for time-harmonic elastodynamics of unbounded domains: theory and finite-element implementation," Comput. Methods Appl. Mech. Eng. **192**(11-12), 1337–1375 (2003).
37. A. K. Naik, M. S. Hanay, W. K. Hiebert, X. L. Feng, and M. L. Roukes, "Towards single-molecule nanomechanical mass spectrometry," Nat. Nanotechnol. **4**(7), 445–450 (2009).
38. M. Li, H. X. Tang, and M. L. Roukes, "Ultra-sensitive NEMS-based cantilevers for sensing, scanned probe and very high-frequency applications," Nat. Nanotechnol. **2**(2), 114–120 (2007).
39. M. Poot and H. S. J. van der Zant, "Mechanical systems in the quantum regime," Phys. Rep. **511**(5), 273–335 (2012).
40. Y. Akahane, T. Asano, B.-S. Song, and S. Noda, "Fine-tuned high-Q photonic-crystal nanocavity," Opt. Express **13**(4), 1202–1214 (2005).
41. X. Yang, M. Yu, D.-L. Kwong, and C. W. Wong, "All-optical analog to electromagnetically induced transparency in multiple coupled photonic crystal cavities," Phys. Rev. Lett. **102**(17), 173902 (2009).
42. T. Asano, B.-S. Song, and S. Noda, "Analysis of the experimental Q factors (~ 1 million) of photonic crystal nanocavities," Opt. Express **14**(5), 1996–2002 (2006).
43. S. G. Johnson and J. D. Joannopoulos, "Block-iterative frequency-domain methods for Maxwell's equations in a planewave basis," Opt. Express **8**(3), 173–190 (2001).
44. J. Gao, J. F. McMillan, M.-C. Wu, J. Zheng, S. Assefa, and C. W. Wong, "Demonstration of an air-slot mode-gap confined photonic crystal slab nanocavity with ultrasmall mode volumes," Appl. Phys. Lett. **96**(5), 051123 (2010).

45. B.-S. Song, T. Asano, Y. Akahane, Y. Tanaka, and S. Noda, "Transmission and reflection characteristics of in-plane hetero-photonic crystals," Appl. Phys. Lett. **85**(20), 4591–4593 (2004).
46. A. F. Oskooi, D. Roundy, M. Ibanescu, P. Bermel, J. D. Joannopoulos, and S. G. Johnson, "MEEP: A flexible free-software package for electromagnetic simulations by the FDTD method," Comput. Phys. Commun. **181**(3), 687–702 (2010).
47. K. Srinivasan and O. Painter, "Momentum space design of high-Q photonic crystal optical cavities," Opt. Express **10**(15), 670–684 (2002).
48. G. Anetsberger, R. Rivière, A. Schliesser, O. Arcizet, and T. J. Kippenberg, "Ultralow-dissipation optomechanical resonators on a chip," Nat. Photonics **2**(10), 627–633 (2008).
49. COMSOL Group, *http://www.comsol.com/*
50. M. Eichenfield, J. Chan, A. H. Safavi-Naeini, K. J. Vahala, and O. Painter, "Modeling dispersive coupling and losses of localized optical and mechanical modes in optomechanical crystals," Opt. Express **17**(22), 20078–20098 (2009).
51. S. G. Johnson, M. Ibanescu, M. A. Skorobogatiy, O. Weisberg, J. D. Joannopoulos, and Y. Fink, "Perturbation theory for Maxwell's equations with shifting material boundaries," Phys. Rev. E Stat. Nonlin. Soft Matter Phys. **65**(6), 066611 (2002).
52. C. W. Wong, P. T. Rakich, S. G. Johnson, M. Qi, H. I. Smith, E. P. Ippen, L. C. Kimerling, Y. Jeon, G. Barbastathis, and S.-G. Kim, "Strain-tunable silicon photonic band gap microcavities in optical waveguides," Appl. Phys. Lett. **84**(8), 1242–1244 (2004).
53. K. Y. Yasumura, T. D. Stowe, E. M. Chow, T. Pfafman, T. W. Kenny, B. C. Stipe, and D. Rugar, "Quality factors in micron- and submicron-thick cantilevers," J. Microelectromech. Syst. **9**(1), 117–125 (2000).
54. Y. Takahashi, Y. Tanaka, H. Hagino, T. Sugiya, T. Sato, T. Asano, and S. Noda, "Design and demonstration of high-Q photonic heterostructure nanocavities suitable for integration," Opt. Express **17**(20), 18093–18102 (2009).

1. Introduction

Cavity optomechanics, a subject studying the coherent interaction of optical and mechanical degrees of freedom of various optical cavities, has been a recent research focus [1–4]. Its applications include laser cooling of mesoscopic systems to their motional quantum mechanical ground state [5–13], photon–phonon translation and storage of light pulses [14–16], and quantum precision measurements of microwave and optical photons [17–19]. Photonic crystals (PhC) are a versatile cavity platform widely used for light–matter and light–structure interactions, e.g., cavity quantum electrodynamics [20,21], nonlinear optics [22–24], and cavity optomechanics [25,26]. Enabled by large optical gradient forces [27–29], high-Q PhC cavities exhibit strong optomechanical interactions in both one-dimensional (1D) [30] and two-dimensional (2D) [31–33] geometries.

In this paper we investigate for the first time the theoretical design of a "nanobeam-in-cavity" and compare the numerical simulation with our recent experimental observations [34]. A nanobeam mechanical resonator is embedded *within* a PhC nanocavity to obtain a small modal mass and large optomechanical coupling. The mechanical modes are localized in a volume smaller than that of the optical modes, with femtogram masses. The mechanical properties are readily and deterministically tuned, and compared with our measurements in the presence of fabrication imperfections [35,36]. The strong optical scattering from the embedded nanobeams requires reengineering of the photonic band structure and fine tuning of the radiation light cone to optimize the optical Q, as supported by our experimental observations. We further analyze the optomechanical coupling for several nanobeam-in-cavity geometries, where the coupling rate $g_{om}/2\pi$ ranging from 4.8 to 15.5 GHz/nm (vacuum optomechanical coupling rate $g_0/2\pi$ of 124.1 kHz to 326.6 kHz) is found in theory and experiment.

2. Optical design: band structure and radiation suppression

Nanobeams are widely used to build high-frequency nanomechanical resonators [37–39]. As shown in Fig. 1, our nanobeam-in-cavity consists of two nanobeams embedded in a PhC slab where three air slots are placed in the region of three missing holes of a triangular lattice. Since a PhC cavity based on three missing air holes in an otherwise perfect triangular lattice is usually referred to as an L3 cavity [40,41], we name ours an "L3-nanobeam cavity." The nanobeams introduce strong perturbation to the original L3 cavity, resulting in significant modification of the optical characteristics [42]: First, the effective refractive index in the

cavity region is reduced by the slots, which shifts the cavity resonance away from the bandgap and makes it difficult to localize the optical energy in a small volume; Second, the sharp edges of the slots result in a large radiation energy leakage [40]. Careful designs are thus required to restore a high optical Q after introducing the slots. We overcome the adverse effects and optimize the cavity with the following strategies: First, the y distance of w_{wg} is increased, i.e., made wider than the width of a single-missing-row (W1) waveguide, which compensates the effect of reduced effective refractive index. The holes in the cavity row are enlarged accordingly to provide a reliable in-plane field confinement in the x direction. The holes surrounding the cavity are shifted to tune the optical field profile such that the vertical radiation scattering is minimized [40]. Numerical modeling proved the effectiveness of the above implementations and that the optical field of this L3-nanobeam cavity is indeed different from that of a regular L3 cavity [40]. For simplicity, it is straightforward to construct symmetric structures with $w_b = w_{b1} = w_{b2}$ and $w_{as} = w_{as1} = w_{as2} = w_{as3}$.
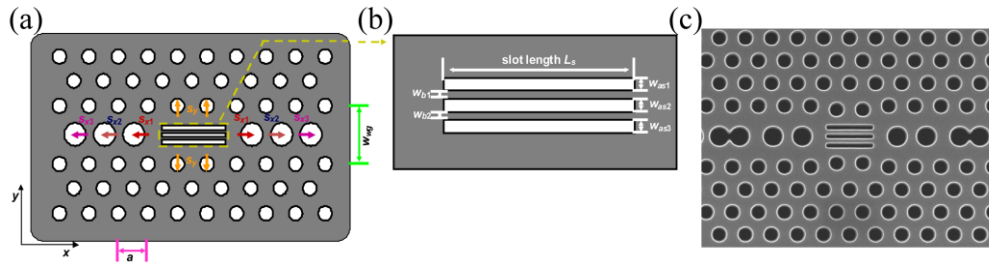

Fig. 1. Geometry of the L3-nanobeam cavity. (a) Overview of the device. (b) Zoom-in of the beam region. a is the lattice constant of the triangular PhC; s_{x1}, s_{x2}, and s_{x3} are the hole offsets in the x direction; s_y is the hole offset in the y direction; w_{b1} and w_{b2} are beam widths; w_{as1}, w_{as2}, and w_{as3} are slot widths. (c) Scanning electron micrograph of a fabricated beam-cavity.

The intrinsic properties of different regions of the L3-nanobeam structures are studied by band structure analysis with MPB [43], a vectorial eigensolver of Maxwell's equations with periodic boundary conditions computed by preconditioned conjugate-gradient minimization of the block Rayleigh quotient in a planewave basis. It is well known that the localized modes of a regular L3 cavity can be viewed as Fabry–Pérot modes from a guided TE-like y-odd band of a W1 waveguide. (Note that here "y-odd" refers to the odd (phase = −1) mirror symmetry with respect to the $y = 0$ plane for the *vector* fields.) Similarly, the optical modes of the L3-nanobeam cavity are also based on a slotted waveguide band. Figure 2(a) shows the band structure of the TE-like modes for the PhC lattice, where a quasicomplete bandgap covers the C band and provides confinement for the optical field in the y direction. Figure 2(b) shows the band structure of the slotted waveguide for the TE-like y-odd waveguide modes, where solid and dashed lines correspond to $(w_{as}, w_b) = (60\text{ nm}, 80\text{ nm})$ and $(w_{as}, w_b) = (60\text{ nm}, 60\text{ nm})$, respectively. The waveguide width w_{wg} is selected to be $1.35 \times \sqrt{3}a$, allowing the slot waveguide band to be well located at the center of the PhC bandgap. Figure 2(c) shows the mode-edge frequency versus the waveguide width w_{wg}. The gray regions indicate the slab mode continua of the PhC lattice. A regular W1 waveguide has a propagating TE-like y-odd band inside the PhC bandgap; however, when the slots are introduced, the slotted W1 waveguide band shifts up, pushing its bandedge into the upper PhC slab continuum. By increasing w_{wg} from $\sqrt{3}a$ to $1.35 \times \sqrt{3}a$, the waveguide band moves back to the center of the bandgap and the optical field is guided again by the nanobeam PhC waveguide [Fig. 2(d) and 2(e)]. The E_y field is highly localized inside the slots, similar to that of other air-slot PhC waveguides [44]. The intensity $|E_y|^2$ across the waveguide is shown in Fig. 2(f), where the origin ($y = 0$) denotes the center of the middle slot. The boundary conditions result in sharp slopes at the air–silicon interfaces. The three peaks correspond to the highly concentrated field inside the three slots. The center peak is weaker than the outer ones, providing an

asymmetry across the silicon nanobeams, a prerequisite for taking advantage of the gradient optical force for related beam motions [27].
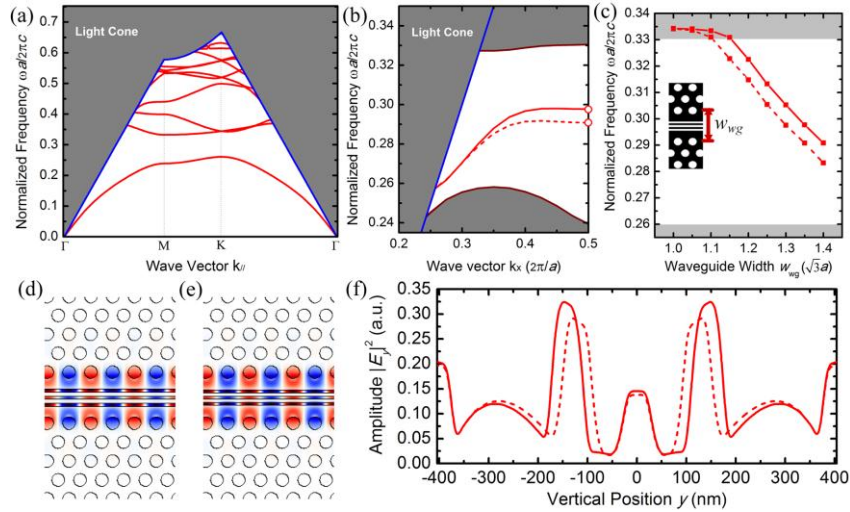

Fig. 2. (a) TE-like bands of a PhC slab with a triangular lattice of air holes where lattice constant a = 430 nm, hole radius r = 0.29a, refractive index of silicon n_{si} = 3.48, and silicon slab thickness h = 220 nm. (b) TE-like y-odd waveguide band for the slotted W1.35 waveguide with w_{wg} = 1.35 × $\sqrt{3}a$, (w_{as}, w_b) = (60 nm, 80 nm) (red solid line) and (w_{as}, w_b) = (60 nm, 60 nm) (red dashed line). Red circles indicate the bandedges. (c) Waveguide bandedge frequency versus the waveguide width w_{wg}. The gray regions indicate the PhC slab mode continua. The inset illustrates the geometry. (d),(e) Field distribution of E_y at the bandedge as indicated by the upper and lower red circles in (b), respectively. (f) E_y intensity profile along the y direction, i.e., perpendicular to the slots. The solid line is obtained from (d) and the dashed from (e), cut from center of the hot optical spots.
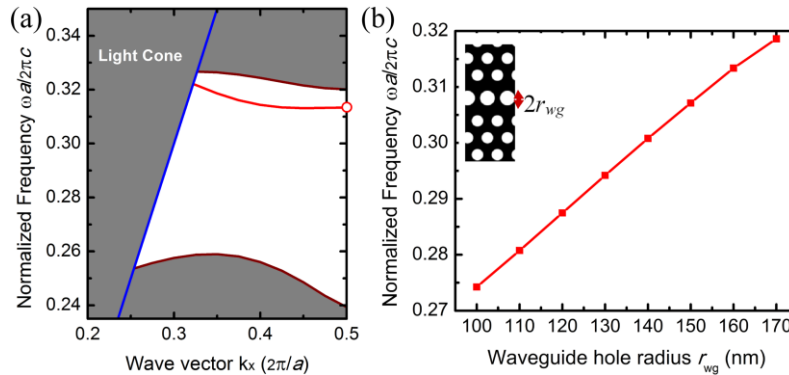

Fig. 3. (a) Band structure of the TE-like y-odd band for the "mirror" waveguide with hole radius r_{wg} = 160 nm. (b) Waveguide bandedge frequency versus the waveguide hole radius r_{wg}. The inset illustrates the geometry.

Next, to create a cavity mode, we confine the field in the x direction by replacing the infinitely long slots with ones of the planned beam length, surrounded by "mirror" air holes [45]. Figure 3(a) shows the TE-like y-odd guided band for the "mirror" waveguide with hole radius r_{wg} = 160 nm. Figure 3(b) shows that the edge of this guided band is pushed up by using a larger radius. Comparing Fig. 3(a) and Fig. 2(b), we find that the band of the "mirror" waveguide sits well above that of the slot waveguide. Their zero overlap in frequency range is important for suppressing the optical energy leakage via the "mirror" waveguide. Based on the above guidelines, a selected set of geometrical parameters are: (a, r, h, w_{wg}, r_{wg}) = (430

nm, 0.29a, 220 nm, W1.35, 160 nm), which are used for further optimization of the cavity mode.
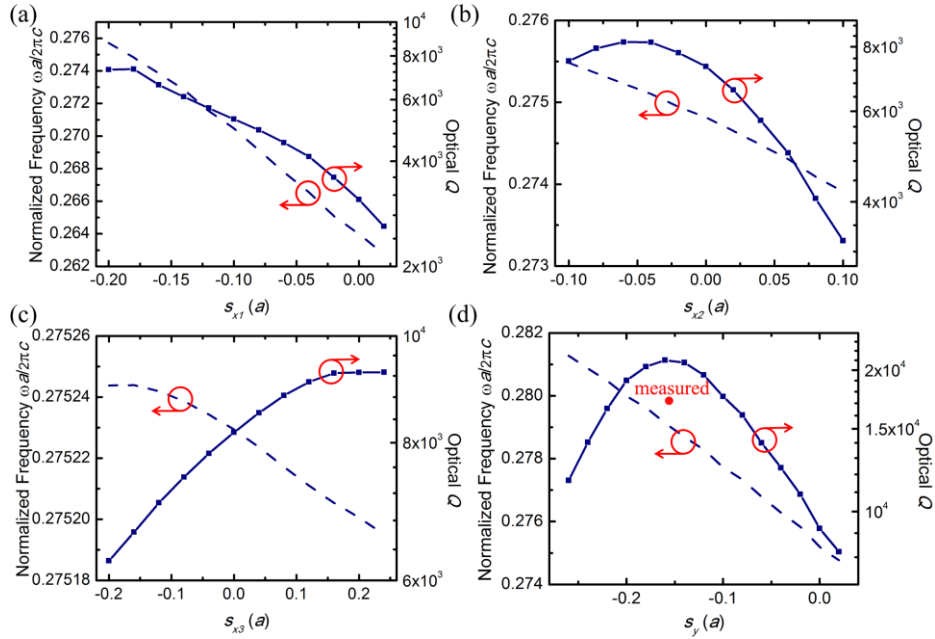

Fig. 4. Optimization process for the cavity with (w_{as}, w_b) = (60 nm, 80 nm) by tuning hole positions of s_{x1}, s_{x2}, s_{x3}, and s_y respectively in series, as shown in panels (a) to (d). For an air slot length L_s of 1.8a, the maximum optical Q of 1.95×10^4 is achieved with (s_{x1}, s_{x2}, s_{x3}, s_y) = (−0.18a, −0.06a, 0.22a, −0.15a) [Design 1]. With a similar optimization process, cavities with (w_{as}, w_b) = (60 nm, 60 nm) achieve a higher optical Q of 5.22×10^4 with (L_s, s_{x1}, s_{x2}, s_{x3}, s_y) = (1.9a, −0.3a, −0.02a, 0.1a, 0) [Design 2]. Solid lines indicate the optical Q, while the dashed lines indicate the normalized resonant frequency. The red dot in Panel (d) indicates the measured unloaded optical Q of the nanobeam cavity based on Design 1 from experiments.

From the band structure design and calculations, we have created a localized cavity made by ensuring the in-plane modal confinement. In what follows we use finite-difference time-domain (FDTD) method to simulate the L3-nanobeam cavities [46] and optimize their optical Q by shifting the surrounding holes iteratively [40]. This will further suppress the excess radiation loss caused by the sharp transitions at cavity edges. A spatial resolution of 21.5 nm is used in combination with subpixel averaging. The starting optical Q for nanobeams with (w_{as}, w_b, L_s) = (60 nm, 80 nm, 1.8a) is around 2.0×10^3. As shown in Fig. 4(a), shifting the adjacent holes towards the nanobeams with $s_{x1} = -0.18a$ increases the optical Q to 7.3×10^3. Further tuning of s_{x2}, s_{x3}, and s_y leads to an optical Q of 1.95×10^4. This optimized geometry with hole offsets (s_{x1}, s_{x2}, s_{x3}, s_y) = (−0.18a, −0.06a, 0.22a, −0.15a) will be subsequently referred to as "Design 1." It is worth noting that s_y is not trivial in this L3-nanobeam cavity design: a variation of s_y from 0 to −0.15a actually doubles the optical Q. Based on Design 1, we fabricated the devices [34] and observed experimental optical Q values around 10^4. The highest experimental loaded optical Q is 1.5×10^4 and the corresponding unloaded Q is 1.7×10^4 as inferred from the normalized on-resonance transmission of 0.015. This experimental value is marked in Fig. 4(d) for comparison and its deviation from the simulation is due to surface roughness scattering in the fabricated samples. Following a similar optimization process, cavities with thinner nanobeams (w_{as}, w_b, L_s) = (60 nm, 60 nm, 1.9a) exhibit an even higher optical Q of 5.22×10^4 with hole offsets (s_{x1}, s_{x2}, s_{x3}, s_y) = (−0.3a, −0.02a, 0.1a, 0), which will be subsequently referred to as "Design 2". We note that this is over two orders-of-magnitude improvement over conventional W1 L3-nanobeam cavities without tuning the w_{wg}

nor the cavity parameters. These two designs with different beam geometries demonstrate the achievable high optical Q of such L3-nanobeam cavities.

To further investigate the cavity mode, the modal distributions of the E_y component for different Q values are analyzed using spatial Fourier transform (FT) [40] as shown in Fig. 5. The fields have an odd symmetry in the x direction, leading to a negligible portion inside the radiation light cone as indicated by the red circles [47]. Spatial components at $K_x \approx 0$ of the leaky fields are thus greatly suppressed. From Fig. 5(d) to 5(f), the leaky components inside the light cone are reduced as the optical Q increases. This indicates that the enhanced optical Q during the optimization process results not only from a smoother field profile but also from a more delocalized field [see Fig. 5(a)–5(c)]. The optical modal volumes for the two designs in Fig. 5(b) and 5(c) are 0.079 μm^3 and 0.12 μm^3, or 0.021 $(\lambda_0/n_\text{air})^3$ and 0.032 $(\lambda_0/n_\text{air})^3$ respectively, where λ_0 is the free-space resonant wavelength and n_air is the refractive index of air. The small optical modal volumes compared to other high-Q PhC cavities [40] are actually a result of predominantly localized modal energy inside the air slots.
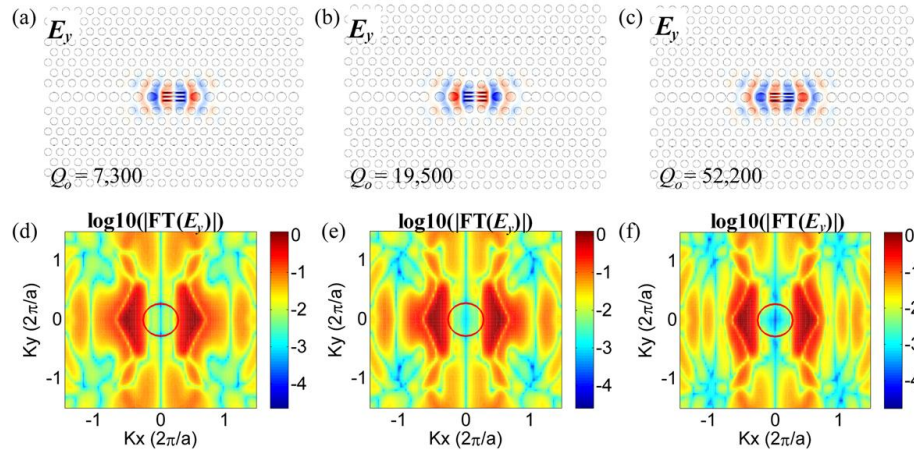

Fig. 5. (a)–(c) Modal distribution of the E_y field. (d)–(f) Corresponding spatial Fourier transformation (FT) for cavities with increasing optical Q. (a) and (d) correspond to $(L_s, s_{x1}) = (1.8a, -0.18a)$ in Fig. 4(a) with an optical Q of 7.3×10^3. (b) and (e) correspond to the optimized geometry Design 1. (c) and (f) correspond to the optimized geometry Design 2.

3. Mechanical design: eigenmodes and elastic radiation leakage

Doubly clamped beams have been widely used to build mechanical resonators [37–39]. Their high mechanical quality factor Q_m and mechanical frequency f_m are very useful for optomechanical applications, such as mass sensing, force sensing, and cooling/amplification of mechanical vibrations [48]. Depending on specific geometry, the frequency of the silicon nanobeams used here is around 1 GHz for the fundamental in-plane mode. The mechanical Q is affected by various loss mechanisms, e.g., clamping, thermoelastic damping, defect motions, and fluidic loss, etc. Among all the sources, clamping loss is usually a major loss channel for doubly clamped beams [39]. We compute the complex frequencies of mechanical modes of the L3-nanobeam cavity with the eigenvalue module in COMSOL 4.2a, a multiphysics solver based on a finite-element method [49]. The mechanical Q is then easily derived. The simulated geometry is identical to that used in the optical modeling. PMLs are applied at the boundaries of computation domain as an efficient impedance-matched nonphysical material for absorbing the radiating elastic waves without reflection [35,36,50]. Its implementation is based on complex coordinate scaling and has also been widely used in electromagnetic simulations [46]. The outer edges of the PMLs are fixed, and the thickness of the PMLs is set approximately to one elastic wavelength. As shown in Fig. 6(a), the minimum mesh element size is 2.4 nm and the mesh element growth rate is 1.3. The maximum mesh

element size is 20 nm in the beam region and 60 nm in other regions. The resolution of the curvature is 0.2. With these settings, every mesh element is thus at least 89 times smaller than the wavelengths of the transverse and longitudinal elastic waves, which are 9.66 μm and 5.34 μm, respectively, in silicon at 1 GHz. The effectiveness of absorption by the PMLs is confirmed [36] by applying harmonic point forces to a photonic crystal membrane.
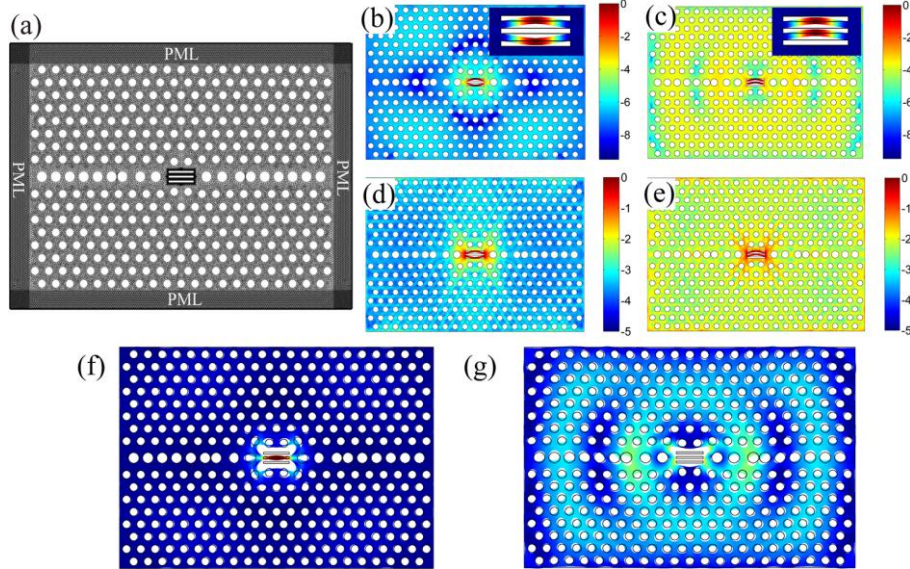

Fig. 6. (a) Top view of the meshed structure used in the finite-element analysis. Fixed boundary conditions are applied outside the PMLs. The top and bottom surfaces are set as free boundaries. (b),(c) Normalized displacement field intensity (log scale) for the differential and common mode of Design 1, respectively. The insets are zoom-ins of the localized beam motion showing the displacements in linear scale. (d),(e) Corresponding von Mises stress field (log scale). (f) Radiating longitudinal elastic wave excited by the differential beam motion (Media 1). (g) Radiating transverse wave excited by the common beam motion (Media 2). In (f) and (g), the displacement fields (linear scale) are overlaid with structural deformation.

Figure 6 illustrates the in-plane mechanical modes of the nanobeams. For the L3-nanobeam cavity, the two nanobeams are clamped to the pliant PhC slab and are thus mechanically coupled via the anchors, resulting in a differential and a common mode [30]. For Design 1, the computed complex frequencies f_m of these eigenmodes are $9.61 \times 10^8 + i4.24 \times 10^4$ Hz and $9.58 \times 10^8 + i9.94 \times 10^6$ Hz, respectively. These compare well with an analytical estimate from $f_m = C\sqrt{E/\rho}\left(w_b/L_s^2\right)$ [39], where the Young's modulus E is 170 GPa and the density ρ is 2330 kg/m^3 for single-crystal silicon. C is a constant dependent on the mode and the beam clamping conditions at the ends of the beam. For the fundamental mode of a doubly clamped beam, $C = 1.07$ (for a Poisson's ratio of 0.28) and the estimated frequency is 1.2 GHz for a beam with the dimensions of Design 1, which is slightly higher due to the finite mechanical compliance at the clamping points in the COMSOL computations.

Furthermore, we note that the clamping-loss-limited mechanical Q for the differential mode (1.13×10^4) is more than two orders of magnitude higher than that for the common mode (only 48). This significant Q difference can be explained by the mechanical displacement field and stress field as shown in Fig. 6(b)–6(g). Figure 6(b) and 6(c) are snapshots of the mechanical displacement intensity (log scale) for the differential and common modes. The displacement intensity is defined as $I = \sqrt{\operatorname{Re}(u)^2 + \operatorname{Re}(v)^2 + \operatorname{Re}(w)^2}$ where u, v, and w are the displacements in the x, y and z directions, respectively. The difference resides not only in the beam motion but also in the radiating elastic waves

propagating in the PhC membrane: First, the amplitude of the radiating elastic waves for the differential mode is much smaller than that for the common mode, which directly explains the much higher Q of the differential mode than the common mode. Second, the radiation pattern for the common mode is similar to that produced by an in-plane harmonic point force driving the membrane in the y direction, while the radiation pattern for the differential mode is more interference-like. The loss channels are also different for these two modes, as illustrated by the stress fields in Fig. 6(d) and 6(e). The differential mode has much more localized field around the anchor region than the common mode. This is attributed to the fact that the two nanobeams pull the anchors in opposite directions for the differential mode, whereas they pull in the same direction for the common mode. The different forces induce the excited elastic waves with different phases for the two modes. Further inspection of the propagating elastic waves reveals their different nature. As shown in Fig. 6(f) and 6(g) (movies attached separately), the lattice holes move along the propagation direction for the differential mode, but move laterally with respect to the propagation direction for the common mode. This indicates that longitudinal waves are excited by the differential beam motion while transverse waves are excited by the common beam motion, which are in agreement with their different stress fields. The above investigation points to a greatly suppressed radiation loss for the differential mode. In parallel with the numerical designs, we measured the fabricated samples of Design 1 [34] which show mechanical Q values up to 1230 in vacuum [34]. The discrepancy in the Q values is mainly caused by fabrication imperfections, as illustrated in detail in Section 4.
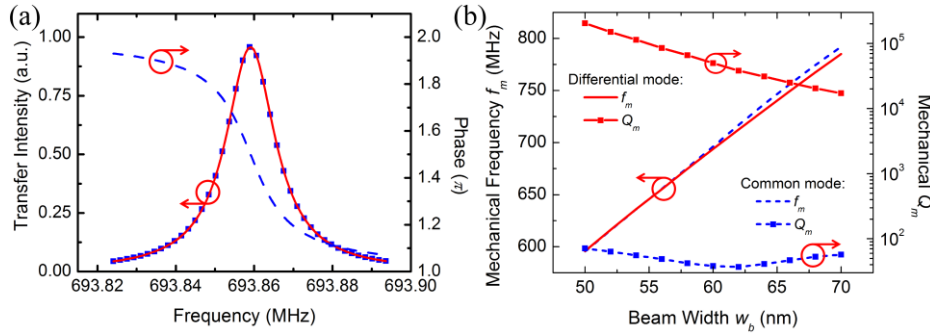

Fig. 7. (a) Transfer function obtained by forced frequency−response analysis. The phase, the transfer intensity, and its Lorentzian fit are plotted in blue dashed line, blue square markers, and red solid line, respectively. (b) Mechanical frequency f_m and quality factor Q_m versus the beam width for both the differential and common mode. Design 2 with w_b = 60 nm is used here.

Compared with Design 1, Design 2 employs thinner and longer nanobeams $(w_b, L_s) = (60$ nm, $1.9a)$. The simulated frequency is 693.9 MHz for the differential mechanical mode, about 268 MHz lower than that of Design 1. The mechanical Q calculated from the complex frequency is 4.99×10^4, more than four times higher than that of Design 1. Its transfer function between the force and displacement obtained from the frequency−response module in COMSOL 4.2a is shown in Fig. 7(a). A harmonic point force oscillating along the y direction is applied at the center of one beam, where the displacement amplitude is also monitored. The transfer intensity is the peak-normalized square of the displacement amplitude and a mechanical Q of 4.53×10^4 is obtained by the Lorentzian fitting, which matches well (within 9%) with that from the complex-frequency computations. Similarly, the mechanical Q fitted from the transfer intensity of Design 1 is 1.09×10^4, which also matches well (within 4%) with that derived from the complex frequency (1.13×10^4). The small discrepancies arise from the computational errors between different solvers. The π-phase transition across the resonance also provides the mechanical Q from its maximum phase slope $2Q_m/f_m$, which is essentially the same as the fitted value from transfer intensity. The transfer function method thus confirms the results obtained by the eigenvalue solver, albeit more computational

intensive. The above numerical results from two different designs have shown a large frequency tuning range and a strong dependence of mechanical Q on the beam width. Such dependence is exhibited in Fig. 7(b), where the beam width varies from 50 to 70 nm for Design 2. The mechanical frequencies change linearly with a slope of 9.45 MHz/nm and 9.91 MHz/nm for the differential and common mode, respectively. The slight difference between their slopes is a result of varying mechanical coupling strength of the two beams: wider beams with larger elastic constant exert larger forces to the clamping points yielding stronger coupling and larger frequency difference. The L3-nanobeam cavities possess high frequencies for beam width w_b less than 100 nm with a linear frequency dependence on w_b according to $f_m \propto w_b/L_s^2$. Furthermore, the mechanical Q increases from 1.72×10^4 to 2.03×10^5 as the beam width decreases from 70 to 50 nm. This is most likely due to the fact that beams with a smaller elastic constant and a smaller mass apply less force to the anchor region and that the stress field is more localized with a reduced beam cross-sectional area. These two factors lead to weaker residual loss (and thus higher Q) for the differential modes, while they do not affect much on the common mode Q. It should be noted that, even with the beam width variation, the optical Q values remain above 4.36×10^4 as shown in Table 1. The overall resonant wavelength shift is about 19 nm, corresponding to an average of 0.95 nm per 1 nm increase in beam width.

4. Dispersive optomechanical coupling and influence of beam asymmetry

In the L3-nanobeam cavities, the optical and mechanical modes are mutually coupled. The optical gradient force created by the injected photons inside the cavity modifies the static positions and dynamic response of the mechanical beams, while the nanobeams vibration changes the phase of the optical cavity field producing a shift of the optical resonance. Both these effects are directly related to an optomechanical coupling rate, which characterizes the strength of optomechanical transductions [1,39]. The dispersive optomechanical coupling rate is defined as $g_{om} = d\omega_o/dx$ where ω_o is the angular frequency of the optical mode and x represents the amplitude of the mechanical motion. The corresponding vacuum optomechanical coupling rate is defined as $g_0 = g_{om}x_{zm}$, where x_{zm} is the zero-point motion of the mechanical mode given by $x_{zm} = \sqrt{\hbar/2m_{eff}\Omega_m}$ with m_{eff} the effective modal mass and Ω_m the angular mechanical frequency ($2\pi f_m$). For regular cavities like microtoroids, microdisks, and Fabry–Pérot etalons, g_{om} is easily determined from their characteristic lengths [1]. For cavities with complicated geometries like our L3-nanobeam cavities, g_{om} is numerically calculated based on the unperturbed optical and mechanical fields by using first-order perturbed solutions of Maxwell's equations with shifting boundaries [51,52]. Reference [30] provides an expression with consistent definitions of effective modal volume V_m and mass m_{eff}. Table 1 lists all the numerical results, where two features are worth noting: For different designs, the common mode always has slightly larger V_m and m_{eff} than the differential mode due to the mechanical mode delocalization as previously discussed. The $g_{om}/2\pi$ for the common mode is zero, since the effective refractive index of the cavity region does not change, to the first order, with the in-plane beams' motion as dictated by symmetry. Properties for two example structures based on Design 2 in Fig. 7(b) are also included in Table 1. The structure with $w_b = 50$ nm possesses the smallest effective mass, while the one with $w_b = 70$ nm achieves the maximum optomechanical coupling rate. Due to their high optomechanical coupling and high mechanical Q, the differential modes can easily be detected by optical transduction in experiments [27,30,34].

Variations from fabrication: So far we have been focusing on symmetric structures with two identical beams. As both nanobeam width and slot width are below 100 nm, tiny variations from the ideal design can cause deviation from the expected properties. To evaluate such effects from, e.g., fabrication imperfections, the center slot of Design 1 is shifted laterally such that the two nanobeams now have different beam widths. Figure 8(a) shows that the higher-frequency mode (Mode 1) originates from the differential motion of the two beams and thus exhibits a higher mechanical Q than the lower-frequency mode (Mode 2) until the

center slot shift s_c reaches 2.0 nm. Note that the mechanical Q of Mode 1 drops to around 1,000 with $s_c = 0.25$ nm, i.e., only a 0.5 nm difference in the beam width. It continues to drop to around 100, similarly to that of Mode 2 when s_c is larger than 1.0 nm. The decoupling of the two beams with increased s_c is also reflected by the beam frequencies, both of which exhibit a linear dependence for s_c larger than 0.5 nm, each approaching the frequency of an individual beam. When s_c reaches 3.0 nm, the frequency difference between the two branches is as large as 50.8 MHz. Figure 8(b)–8(e) show the displacement fields of the nanobeams for the two modes with $s_c = 0.25$ nm (b,c) and $s_c = 3.0$ nm (d,e). The coupled and uncoupled beam motions are evident, which is consistent with the frequency behavior shown in Fig. 8(a). It should be noted that such a 3-nm lateral shift of center slot only slight changes the optical Q, but considerably alters the optomechanical coupling rates for both mechanical modes to approximately one half of that of the differential mode of Design 1 [see Table 1].
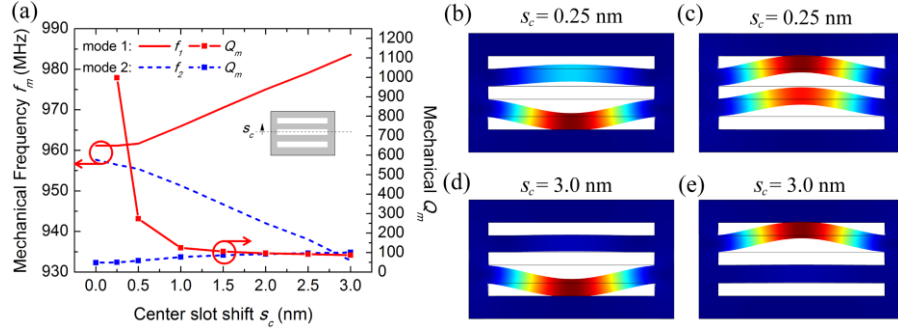

Fig. 8. (a) Mechanical frequency f_m and quality factor Q_m versus the center-slot displacement s_c. Design 1 corresponds to the structure with $s_c = 0$. Mode 1 originates from the differential mode, while Mode 2 originates from the common mode. (b)–(e) Zooms of the displacement fields of the nanobeams with $s_c = 0.25$ nm (b,c) and $s_c = 3.0$ nm (d,e).

Table 1. Optomechanical properties of the L3-nanobeam cavities. Design 1 and Design 2 refer to the two structures obtained in optical Q optimization for different beam geometries.

Structure[a]	λ_0 (nm)	Q_o	Mode	f_m (MHz)	Q_m	V_m (μm^3)	m_{eff} (fg)	$g_{om}/2\pi$ (GHz/nm)	$g_0/2\pi$ (kHz)
Design 1	1541.7	1.95×10^4	*Diff.*	961.2	1.13×10^4	0.011	26.5	11.3	204.6
			Com.	957.7	48	0.013	29.5	~0	~0
Design 2	1553.2	5.22×10^4	*Diff.*	693.9	4.99×10^4	0.0087	20.4	10.9	265.4
			Com.	696.1	38	0.0093	21.6	~0	~0
Bm50nmD2	1543.1	4.36×10^4	*Diff.*	595.9	2.03×10^5	0.0072	16.8	6.8	197.6
			Com.	595.5	71	0.0074	17.2	~0	~0
Bm70nmD2	1562.2	5.32×10^4	*Diff.*	785.0	1.72×10^4	0.0103	24.1	15.5	326.6
			Com.	792.0	57	0.0112	26.2	~0	~0
Shft3nmD1	1540.8	1.94×10^4	*1*	983.6	87	0.0063	14.7	6.1	145.6
			2	932.8	101	0.0058	13.4	4.8	124.1
HiQ48nm	1586.2	1.02×10^5	*Diff.*	574.9	1.17×10^5	0.0064	15.0	13.3	414.3
			Com.	575.3	79	0.0070	16.3	~0	~0

[a]All the structures are formed on silicon slabs with $(a, r, h, w_{wg}, r_{wg})$ = (430 nm, 0.29a, 220 nm, W1.35, 160 nm). Design 1 has $(w_{as}, w_b, L_s, s_{x1}, s_{x2}, s_{x3}, s_y)$ = (60 nm, 80 nm, 1.8a, –0.18a, –0.06a, 0.22a, –0.15a). Design 2 has $(w_{as}, w_b, L_s, s_{x1}, s_{x2}, s_{x3}, s_y)$ = (60 nm, 60 nm, 1.9a, –0.3a, –0.02a, 0.1a, 0). Bm50nmD2 and Bm70nmD2 are variations of Design 2 with beam width $w_b = 50$ nm and 70 nm respectively, which correspond to the two extrema of w_b in Fig. 7(b). Shft3nmD1 is a variation of Design 1 with the center slot shifted by 3.0 nm, corresponding to the structure studied in Fig. 8(d)–(e). HiQ48nm is an design with thinner beams and higher optical Q. It has $(w_{as}, w_b, L_s, s_{x1}, s_{x2}, s_{x3}, s_y)$ = (48 nm, 48 nm, 1.9a, –0.335a, –0.085a, 0.115a, 0).

Table 1 summarizes the optomechanical properties of several typical devices numerically studied in this paper. The experimental results reported in Ref [34]. are in good agreement with the simulation predictions. Fabricated based on Design 1, the sample exhibits a loaded

optical Q of 1.0×10^4, a mechanical frequency around 1 GHz, and a mechanical Q of 1230 in vacuum for the differential mode [34]. The common mode is not observed in the optical transduction measurement due to its small optomechanical coupling rate and a very low mechanical Q. The mode decoupling is also experimentally demonstrated in samples with intentional asymmetry: when the center slot is shifted laterally by 3.0 nm in the layout design, two mechanical peaks are observed with their mechanical Q values both around 55. It is evident that the differential mode of high mechanical Q benefits from the overall symmetry of the double beams. In our simulations here, the higher optical and mechanical Q values are obtained for ideally fabricated structures. In practice, however, the unavoidable structural imperfections during fabrication always deteriorate the device performance. Taking account of the loss to the coupling waveguides, the measured optical Q agrees very well with the simulated value. The optical Q should be further improved by implementation of Design 2 where a 4-fold enhancement is expected. Actually, cavities with thinner beams generally possess higher optimized Q values due to the weaker perturbation. For example, a cavity (w_{as}, w_b, L_s, s_{x1}, s_{x2}, s_{x3}, s_y) = (48 nm, 48 nm, 1.9a, $-0.335a$, $-0.085a$, 0.115a, 0), labeled as "HiQ48nm" in Table 1, exhibits an optical Q of 1.02×10^5. On the mechanical part, we have observed a drop of mechanical Q from 1230 in vacuum to 580 in air [34]. It is clear that air damping plays a major role in ambient conditions. Under vacuum conditions, while the mechanical Q of devices reported by other groups [5,6,53] is limited by thermoelastic damping (TED), the TED-limited mechanical Q of our devices is estimated by COMSOL to be 7.08×10^4 for the fundamental differential mode of Design 1 at room temperature [49]. Under cryogenic conditions, the Q value is even larger [5,6]. Thus, it is safe to exclude TED as the main loss mechanism. On the other hand, since the significant Q drop and mode decoupling of center-slot-shifted cavities are well predicted by analysis in Fig. 8, it is concluded that clamping loss should be the main loss mechanism for our devices measured in vacuum and the relatively low measured Q values are basically due to the uncontrollable fabrication imperfections.

5. Conclusions

We have numerically demonstrated a novel L3-nanobeam cavity, which consists of two mechanical nanobeams embedded in a PhC membrane where three holes are removed. 3D modeling with PMLs is employed for both optical and mechanical simulations. With *ab initio* calculation and comprehensive optimization, an optical Q up to 5.2×10^4 is obtained. Designs with optical Q larger than 10^5 are also achieved for cavities with reduced nanobeam widths. The fundamental in-plane mechanical modes of the high-optical-Q designs are also analyzed systematically. The mechanical frequencies approach 1 GHz and can easily be tuned by slightly varying the beam width while maintaining a high optical Q. The anchor-loss-limited mechanical Q for the differential mode is higher than 10^4. The elastic radiation waves are shown to be transverse for the common mode and longitudinal for the differential mode. The effects on mode decoupling and mechanical Q due to the fabrication imperfections are also studied. The optical transduction efficiency of the differential mode is very high with vacuum optomechanical coupling rates over 200 kHz. In principle, an ultrahigh-Q optical cavity can be designed based on the mode-gap effect [54] by engineering the slotted waveguide band shown in Fig. 2. However, the mechanical frequency is expected to be much lower because of the much longer beams. Compared with the single-slot structure with ultrahigh optical Q [30–32], our designs target at highly localized mechanical modes inside a PhC nanocavity and exhibit high mechanical frequencies with femtogram modal masses. Conceptually, the L3-nanobeam cavities represent a new type of nano-optomechanical systems created by directly placing ultrasmall mechanical resonators into a photonic nanocavity. Such femtogram-mass, high-optical-Q, high-mechanical-Q structures are promising for optomechanical applications, especially in the ultrasensitive measurements involving mass, force, and displacement.

Acknowledgments